Contents lists available at ScienceDirect

Journal of Solid State Chemistry

Properties of GdSF and phase diagram of the GdF$_3$ - Gd$_2$S$_3$ system

M.U. Abulkhaev [a,*], M.S. Molokeev [b,c], A.S. Oreshonkov [b,c], A.S. Aleksandrovsky [b,c], A.V. Kertman [a], D.N. Kamaev [d], O.V. Trofimova [a], A.V. Elyshev [a], O.V. Andreev [a,e]

[a] Tyumen State University, Tyumen, Volodarsky str. 6, 625003, Russia
[b] Kirensky Institute of Physics, Federal Research Center KSC SB RAS, Krasnoyarsk, Akademgorodok str. 50, Building 38, 660036, Russia
[c] Siberian Federal University, Krasnoyarsk, Svobodnyj av. 79, 660079, Russia
[d] Department of Physical and Applied Chemistry, Kurgan State University, Sovetskaya str. 63/4, Kurgan, 640020, Russia
[e] Institute of Solid State Chemistry, Ural Branch, Russian Academy of Sciences, Ekaterinburg, Pervomaiskaya str. 91, 620990, Russia

ARTICLE INFO

ABSTRACT

The objectives of this study were to refine the phase diagram of the GdF3-Gd2S3 system and to calculate their liquidus, and to synthesize GdSF and to study their properties. The GdSF compound (ST PbFCl, *P4/nmm*, *a* (Å) 3.83006(17), *c* (Å) 6.8529(3), has an optical band gap for a direct interband transition of 2.56 eV and is characterized by a pronounced increase in the Kubelka-Munk function in the region of this transition. Direct optical bandgap of GdSF is measured to be equal to 2.77 eV. Two indirect bandgaps are detected to be 1.54 and 2.4 eV. Meta-GGA simulations of band structure predicting 1.481 eV direct bandgap of GdSF are in good agreement with these features of the experimental absorption spectrum. To explain this complicated case, we argue that formally direct optical transitions to highly dispersive subbands contribute not to direct but to indirect bandgaps measured by Tauc analysis. The GdSF compound melts incongruently with the formation of a melt and γ-Gd2S3 compound at t = 1280 ± 2°C, ΔH = 40.6 ± 2.8 kJ/mol, ΔS = 26.1 ± 1.8 J/mol*K. The eutectic has a composition of 13 mol.% Gd2S3 (0.74 GdF3 + 0.26 GdSF), the melting characteristics of the eutectic are 1182 ± 2°C, ΔH = 36.2 ± 2.5 kJ/mol, ΔS = 24.9 ± 1.7 J/mol*K. In the system GdF3 - Gd2S3 the balance equations for five phase transformations recorded by the DSC method were compiled. Convergence was achieved in the liquidus of the system constructed according to DSC data and calculated with the use of the Redlich-Kister equation.

1. Introduction

Compounds of composition LnSF (Ln - La, Ce, Pr, Nd, Sm, Gd, Tb, Dy, Ho, Er, Tm, Yb, Lu) are promising as optical materials, in laser technology [1–4] and electronics [5]. The LnSF compounds are inorganic color pigments, and they have high chemical inertness, thermal stability, wide color range and UV resistance [1–7].

Gadolinium Gd $4f^7$ $5d^1$ $6s^2$ has a half filled 4f level, and electronic configuration of the Gd^{3+} ion is $4f^7$. Oxide and sulfide compounds containing the trivalent gadolinium ion are matrix structures for creating doped optical materials. The refinement of the phase diagram of the GdF$_3$ - Gd$_2$S$_3$ system will make it possible to understand the processes occurring during the synthesis of GdSF samples, and to select methods and conditions for obtaining doped samples. The solubility of REE (rare earth elements) sulfides in REE fluorides was not studied in detail. Information about the diagram is presented in the abstract of the conference [8]. In the GdF$_3$–Gd$_2$S$_3$ system, the GdSF compound decomposes by a peritectic

reaction, temperature at 1282°C (1555 K). No noticeable areas of solid solutions based on the GdF$_3$ and GdSF compounds were found. An eutectic is formed between the GdF$_3$ and GdSF phases at 13 mol. % Gd2S3 and 1157°C (1430 K). The length of solid solutions based on γ-Gd$_2$S$_3$ is 98–100 mol. % at 1427°C (1700 K) [8].

The GdSF compound (1GdF$_3$:1Gd$_2$S$_3$) has a tetragonal structure of the PbFCl type, sp. gr.

P4/nmm with cell parameters e. i.: *a* = 3.8297(1) Å, *c* = 6.8529(2) Å [3,4], *a* = 3.8345(3) Å, *c* = 6.8518(5) Å [9]. As to related compounds, two polymorph modifications are known for GdF$_3$. The low-temperature rhombic modification α-GdF$_3$ of the structural type (ST) β-YF$_3$ is related to space group *Pnma*: *Z* = 4, *a* = 6.5713 Å, *b* = 6.9954 Å, *c* = 4.3932 Å [10,11], *a* = 6.5630(8) Å, *b* = 6.9712(4) Å, *c* = 4.3873(9) Å [11]. At 1074°C [12], the compound transforms into a high-temperature trigonal β-GdF$_3$ modification of the tysonite (LaF$_3$) type, space group *P3c1*, with parameters e. i. *a* = 6.8782(3) Å, *c* = 7.0621(6) Å [11]. The temperature of congruent melting of GdF$_3$ is 1230°C [12,13], 1252°C [14], and the

melting enthalpy is 50.41 kJ/mol [12,13]. It was shown in Ref. [15] that the $GdF_{3-2x}O_X$ solid solution is formed in the GdF_3–Gd_2O_3 system. The dissolution of Gd_2O_3 in GdF_3 is accompanied by an increase in the melting point of the solid solution by 90 °C for the composition $GdF_{2.76}O_{0.12}$.

The low-temperature orthorhombic modification α-Gd_2S_3 crystallizes in the α-La_2S_3 structural type, *Pnma*, $a = 10.7447(7)$ Å, $b = 3.8985(3)$ Å, $c = 10.5446(9)$ Å, $Z = 4$ [16]. The transition α-Gd_2S_3→γ-Gd_2S_3 occurs at 1217°C. The γ-Gd_2S_3 modification is related to the Th_3P_4 structure type, I43d, $a = 8.387$ Å, $Z = 4$ [17].

The LnSF compounds for lanthanides of the cerium subgroup melt congruently: LaSF t = 1440 ± 7°C, ΔH = 45.7 ± 4.6 kJ/mol, CeSF t = 1410 ± 7°C, ΔH = 40.7 ± 4.1 kJ/mol, PrSF t = 1388 ± 7°C, ΔH = 39.7 ± 4.0 kJ/mol, NdSF t = 1381 ± 7°C, ΔH = 40.2 ± 4.0 kJ/mol, SmSF t = 1314 ± 7°C, ΔH = 36.1 ± 3.6 kJ/mol. The SmSF phase decomposes in melt-crystallization cycles [18].

Data on the nature of melting, temperatures, and enthalpies of melting of LnSF compounds for rare earth elements of the yttrium subgroup have not been found in the literature.

It is expedient to combine the experimental study of phase diagrams [19–21] with calculation methods, in particular, the calculation of the liquidus line using the Redlich-Kister equation [22]. Using the equation, the liquidus lines of various types of phase diagrams for various types of chemical systems were calculated [22,23], and convergence was achieved between the experimental and calculated data.

Crystalline compounds LnSF are of great interest due to their electronic structure in which, as predicted in recent article [24], the optical properties must depend on the competition between interband transitions of the charge transfer type, on the one hand, and transitions between 4f states experiencing Mott localization, on the other hand.

The aim of the study is to determine the optical and thermal properties of GdSF, establish the electronic structure of the compound and construct the phase diagram of the GdF_3 - Gd_2S_3 system.

2. Experimental methods

Synthesis of samples. The following initial substances were used: gadolinium oxide Gd_2O_3 (99.99 mol. % Gd_2O_3, TOPLUS China), ammonium thiocyanate (98.9 mol. % NH_4SCN, TOPLUS China), ammonium fluoride (98.9 mol. % NH_4F, TOPLUS China), gaseous argon (99.999% Ar, Kriogen Russia).

Gadolinium trifluoride was obtained by the hydrothermal method by autoclaving gadolinium nitrate in the presence of NH_4F at 120–180°C [25–27]. The gadolinium trifluoride powder was dried at 50 °C, and then the sample was annealed at 370 °C in an atmosphere of ammonium fluoride decomposition products to remove adsorbed water molecules and OH groups. α-GdF_3 was obtained with following characteristics: ST PbFCl, *Pnma*, $a = 6.5714$ Å, $b = 6.9842$ Å, $c = 4.3905$ Å. The α-GdF_3 sample was stored in a desiccator at a residual air pressure of 1000–2000 Pa.

The Gd_2S_3 sample was synthesized under the action of a flow of H_2S and CS_2 on Gd_2O_3 at 1050–1100°C [16]. H_2S and CS_2 were obtained by thermal decomposition of NH_4CNS at 260–270°C [17]. α-Gd_2S_3 was obtained with following characteristics: ST α-La_2S_3, *Pnma*, $a = 7.3397$ Å, $b = 15.2732$ Å, $c = 3.9324$ Å. The γ-Gd_2S_3 modification was formed by the annealing of α-Gd_2S_3 at 1500–1600°C in the sulfur vapor atmosphere. The crystal chemical characteristics of γ-Gd_2S_3 are typical for the Th_3P_4 ST: $a = 8.3859$ Å, $Z = 4$ [28].

More than 17 samples of various chemical compositions have been synthesized in the GdF_3 - Gd_2S_3 system. On the plotting diagram, data on the phase composition of samples annealed at 900 °C, as well as the results of their study by DSC and VPTA methods. The batches of starting materials were ground in an agate mortar and placed in graphite crucibles. Then, each crucible was placed in a quartz ampoule. The ampoule was evacuated to 0.1 Pa and sealed. Then, sample was melted by heating the graphite crucible in a high-frequency current setup. The moment of melting was observed visually. The cycles of transferring the sample to

the melt-crystallization of the sample were repeated up to three or four times. Ampoules with samples were annealed in a muffle furnace at 900 ± 5 °C for up to 500 h. According to the physicochemical analysis, all annealed GdSF samples had a phase composition of 100 mol. % GdSF.

Research methods. X-ray phase analysis (XPA) was carried out with the use of a DRON-7 diffractometer equipped by a source of CuKα radiation (Ni-filter). The scanning step was 0.02° (2θ), and the exposure time was 2 s. The unit cell parameters were determined using the PDWin 4.0 software package and the PDF-4 X-ray file using profiling of diffraction peaks. The accuracy of the unit cell parameter determination was ±0.0001 nm [20,22].

Differential scanning calorimetry (DSC) was performed on a SETARAM Setsys Evolution (TGA–DSC 1600) setup with a PtRh6%-PtRh30% thermocouple using the SETSOFT 2000 data processing software [20,22]. Samples 50 mg weight were placed in evacuated and sealed conical quartz ampoules with a base diameter of 5 mm. The heating-cooling surveys were carried out in an argon flow, and the gas supply rate to the upper part of the chamber was 20 ml/min. The sample heating rate was 10 K/min. The setup is calibrated by the reference points: Zn, $K_2Cr_2O_7$, Ag, Au, Cu. The accuracy of temperature determination in a DSC study up to 1200 °C is ±1.8 K, the enthalpy of phase transformations is ±7%. In the DSC study of temperatures 1200–1350 °C, the sample was placed in an open graphite crucible 5 mm in diameter, 8 mm high, with a wall of 0.3 mm. Temperature accuracy 0.5% of the temperature value, enthalpy - 12% of the enthalpy value. To determine the temperatures of the liquidus line, samples weighing 1–1.5 g were obtained. During the crystallization of the samples from the melt, no separation of the phases of the eutectic and primary crystals (according to the density of the phases) occurred. In the DSC survey at the peak of the thermal effect, the liquidus temperature was taken as the end point of heat absorption in the sample.

Scanning electron microscopy (SEM) was used to determine the elemental composition of samples of the system. The analysis was performed on a Tescan Mira 3 LMU using an energy dispersive attachment. The error in determining the content of elements is ±0.5 wt %.

Microstructural analysis (MSA) was carried out by using polished and etched sections on a METAM LV 31 metallographic microscope. Microhardness was determined on an HMV-G21DT microhardness tester at a load of 490.3 mN (50 g) using the software of the HMV-G instrument. Microhardness was measured on polycrystalline samples.

Diffuse reflection UV spectra were recorded for thin layers of powders in the range of 200–1400 nm using a Shimadzu UV-2600 spectrophotometer (Japan) equipped with an ISR-2600 Plus integrating spherical nozzle [29]. The $BaSO_4$ standard (which was supplied by Shimadzu with the spectrophotometer) was used to measure the diffuse reflectance spectra. The diffuse reflection spectra obtained from thin layers of powders were processed using the Kubelka-Munk function, which was modified for the cases of direct and indirect interband transitions [30]. After constructing a linear approximation for the fundamental absorption region, the linearity regions were chosen in such a way that the Pearson correlation coefficient was 0.999, as, for example, in Ref. [31].

3. Results and discussion

3.1. Crystal chemical parameters of GdSF, phase equilibrium in the GdF_3 – Gd_2S_3 system

The diffraction pattern of the GdSF compound was identified in the tetragonal syngony, ST PbFCl, *P4/nmm*, which agrees with the data of [2]. The gadolinium atom is located in the center of the pentagondodecahedron, and it is surrounded by 5 sulfur atoms and 4 fluorine atoms (Fig. 1, Tables 1 and 2). Therefore this structure was taken as starting model for Rietveld refinement which was performed using TOPAS 4.2 [2]. Asymmetric part of the unit cell contains three atoms in special Wyckoff sites (Gd — 8j, S — 8j and F — 4d), therefore only z-coordinates of Gd, S atoms were refined during Rietveld refinement. Thermal parameters were refined independently and isotropically for each atom.
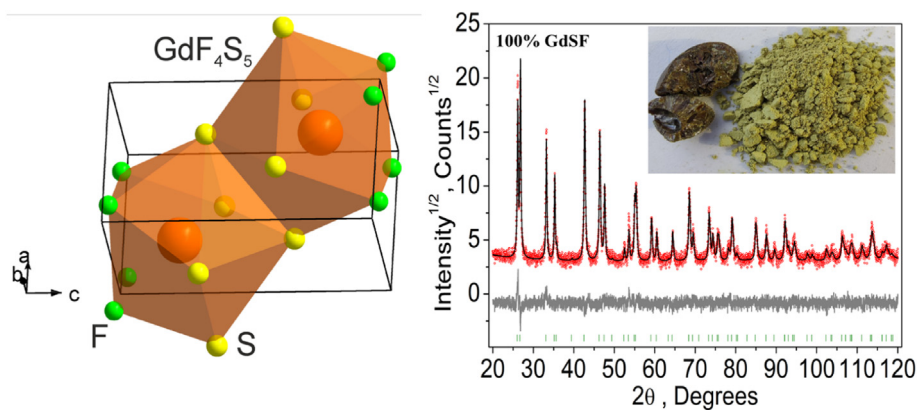
Fig. 1. Crystal structure, Rietveld difference plot and photo of the GdSF sample.

Table 1
Main parameters of processing and refinement of the GdSF samples.

Compound	GdSF
Sp. Gr.	*P4/nmm*
a (Å)	3.83006(17)
c (Å)	6.8529(3)
V (Å3)	100.527(10)
Z	2
2θ-interval, °	20–120
*R*wp,%	15.78
*R*p,%	12.51
χ2	0.71
*R*B,%	6.5

Table 2
Fractional atomic coordinates and isotropic displacement parameters (Å2) of GdSF.

Atom	*x*	*y*	*z*	*Biso*	*Occ.*
Gd	0.25	0.25	0.22990(19)	0.5(2)	1
S	0.25	0.25	0.6536(6)	0.2(2)	1
F	0.75	0.25	0	2.0(4)	1

Refinement was stable and gave low R-factors (Table 1, Fig. 2). Coordinates of atoms and main bond lengths are in Tables 2 and 3 respectively.

In the GdF_3 - Gd_2S_3 system, when substances are in a polycrystalline state in the concentration range 0–50 mol. % Gd_2S_3, the α-GdF_3 and GdSF phases are in equilibrium (Fig. 2 A), as well as β-GdF_3 and GdSF. When quenching ampoules with GdF_3 samples into saline solutions from temperatures of 1100–1150 °C, the α-GdF_3 modification was obtained. Phase transformations of β-$GdF3$ during cooling and quenching of the samples were not detected. In the region of 50–100 mol. % of Gd_2S_3, in the annealing of the samples and their subsequent cooling, the phase states of GdSF and α-Gd_2S_3, GdSF and γ-Gd_2S_3 were found (Fig. 2 B, C). No noticeable solid solutions are formed in the system based on the initial compounds GdF_3, Gd_2S_3. In the two-phase samples of the system, the unit cell parameters of each phase coincided with the unit cell parameters of single-phase samples within the limits of possible determination error (Section Synthesis of samples).

3.2. Calculation of electronic band structure and measurement of GdSF optical bandgap

3.2.1. Calculation details

All density functional theory calculations were performed using CASTEP [32] (Cambridge Serial Total Energy Package) code. The meta-generalized gradient approximation with the on-site orbital dependent Hubbard U energy term [33] and RSCAN [34] (improved version of SCAN [35]) functional were chosen. The best agreement with experimental XPS spectrum [24,36] was achieved with the U_f(Gd) equal to 3 eV. The on-the-fly generated ultrasoft and normconserving pseudopotentials with a cutoff energy equal to 650 and 721.1 eV were used for *meta*-GGA and HSE06 [37] calculations, respectively. The Brillouin zone is sampled by the 5 × 5 × 3 and 3 × 3 × 2 Monkhorst–Pack k-meshes in case of *meta*-GGA and HSE06, respectively. Experimental structural model of GdSF crystal was optimized using *meta*-GGA method until the maximum force became less than 0.01 eV/Å and the maximum stress was smaller than 0.02 GPa [38,39]. The convergence criterion for minimization of total energy was set to be 1×10^{-7} eV [40].

3.2.2. Calculation results and discussion

As the first step of DFT (density functional theory) calculations of GdSF properties, the cell parameters and atom coordinates were relaxed, and the obtained data are presented in Table 3. As can be seen in Table 3, the difference between experimental and DFT optimized structural parameters is less than 1%.

The Brillouin zone (BZ) of GdSF is shown in Fig. 3. The full path along high symmetry points of the BZ should be written as: Γ–X–M–Γ–Z–R–A–Z|X–R|M–A. Coordinates of these points are: Γ(0, 0, 0), X(0, 0.5, 0), M(0.5, 0.5, 0), Z(0, 0, 0.5), R(0, 0.5, 0.5), A(0.5, 0.5, 0.5). It should be noted that electronic structure only along M–Γ–Z–R path only was published previously [24], and the appearance of bands is in general similar both in Ref. [24] and in our calculation. The electronic structure of GdSF calculated by *meta*-GGA is presented in Fig. 3. As the gadolinium is a lanthanide element, a spin up and spin down states shown by different colors. According to the results, it can be supposed that GdSF is a direct band gap semiconductor with $E^d_g = 1.481$ eV. The value of E^d_g obtained with hybrid HSE06 method is equal to 1.686 eV.

Total electronic density of states (DOS) and partial DOS presented in Fig. 4. The comparison of calculated DOS below 0 eV with experimental XPS data [24,36] showed excellent agreement in positions of f-Gd, p-F and p-S bands. According to Fig. 4, the valence band top of GdSF is formed by p-electrons of S, while the conduction band bottom is governed by the Gd d-states. It should be noted that density of states of d-orbital is rather low from the bottom of conduction band (1.481 eV) to 3.25 eV.

The Kubelka-Munk function modified for case of indirect bandgap was built on the base of diffuse reflectance spectrum and is presented in Fig. 5. The optical bandgap obtained via non-modified Kubelka-Munk function is equal to 2.56 eV. The value is very close to the value of 2.5 eV calculated in theoretical article [24] with the help of WIEN2k package and modified Becke-Johnson exchange-correlation potential. However, as it is stressed in a recent study [30], the use of unmodified Kubelka-Munk function can lead to an error, which, in some cases, can be
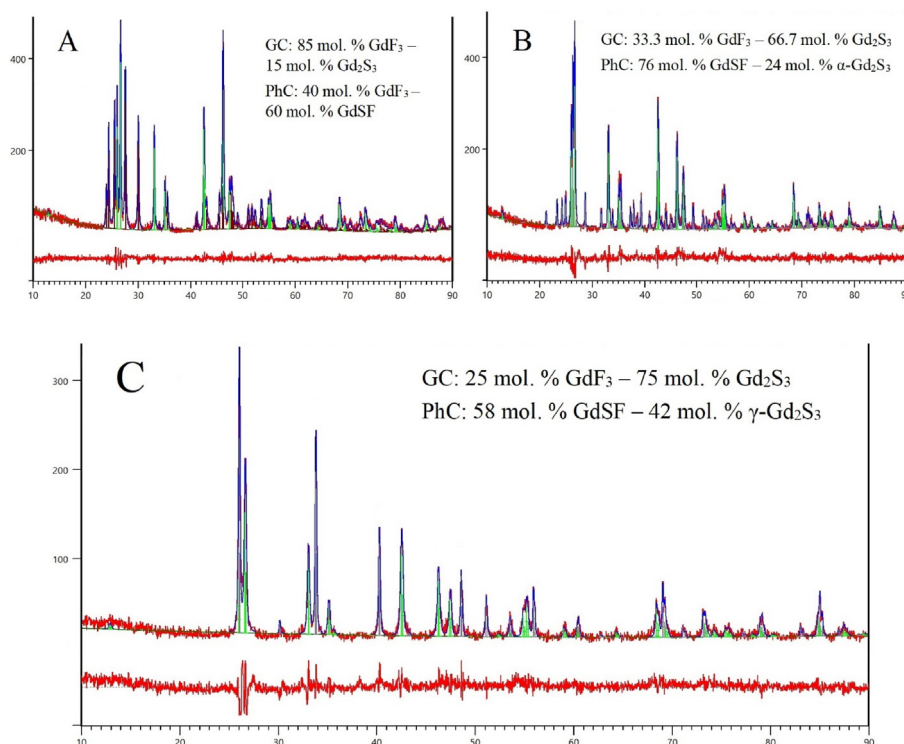
Fig. 2. X-ray diffraction patterns of samples of the GdF_3–Gd_2S_3 system. GC – global composition, PhC – phase composition by XPA.

Table 3

DFT calculated structural parameters for GdSF. Experimental values obtained in this work are presented in parentheses.

Lattice dimensions, Å	a	c	
	3.83006	6.8529	
	(3.85563)	(6.86918)	
Fractional coordinates	x	y	z
Gd	0.25	0.25	0.22799
			(0.22990)
S	0.25	0.25	0.647
			(0.6536)
F	0.75	0.25	0

Fig. 4. Total and partial density of states of GdSF.

significant. In Ref. [30] it is believed that the modification of the Kubelka-Munk function for the cases of direct and indirect transitions, despite its approximate nature, may be preferable. To avoid the misfit between Kubelka-Munk function and the absorption spectra, translucent powder-containing discs can be used, but this approach requires hyper-quality of the personnel [41,42]. Therefore, in our study Kubelka-Munk functions modified according to Ref. [30] allow us to find the direct bandgap in GdSF equal to 2.77 eV, while indirect bandgap is as low as 2.4 eV. At the same time, the growth of fundamental absorption on the plot of Kubelka-Munk function above 2.5 eV has a very pronounced character, which does not agree very well with the band structures presented in figures in Ref. [24]. Really, as it is evident from the band structure calculated in Ref. [24], interband transition in GdSF originates from the excitation of 3p electrons of sulfur to the 5d orbitals of gadolinium. The PDOS of 5d states of gadolinium in the vicinity of interband transition is expected, due to strong dispersion, to be rather low and
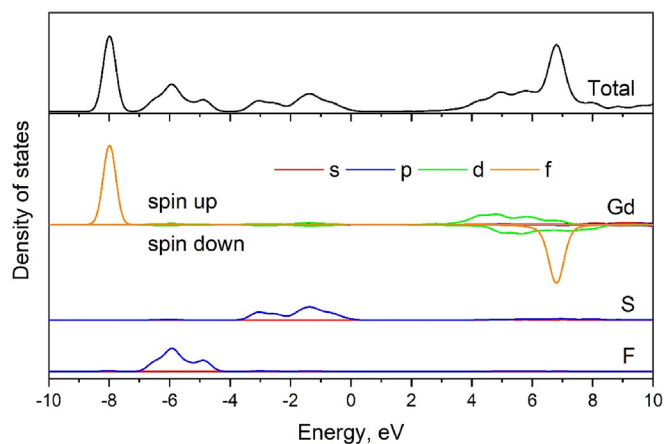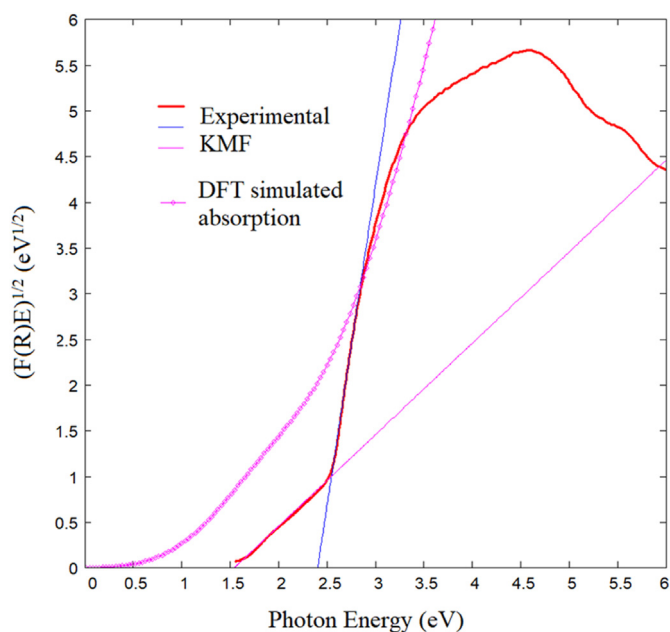

Fig. 3. Electronic band structure of GdSF calculated using the *meta*-GGA RSCAN approach.

Fig. 5. Indirect bandgaps in GdSF determined with the help of modified Kubelka-Munk function in comparison with CASTEP *meta*-GGA RSCAN calculations.

should increase slowly, in certain contradiction with our experiment. Therefore, despite the high level and careful performance of the calculations in Ref. [24], they cannot be considered free from an imperfection.

In order to clarify the situation with the band structure of GdSF, we performed *ab initio* calculations as described above in this very subsection using *meta*-GGA RSCAN and HSE06 approaches. The structural parameters were used as obtained by Rietveld refinement in this study. The parameters of the model were partially adjusted in order to fit the energy levels below Fermi energy to the available XPS data [24], and to reach this, we used fitting of correlation energy. The band structure and PDOS obtained are generally similar to those reported in Ref. [24]. However, with no scissors correction, the energy gap between top of the valence band and the bottom of conduction band was equal to 1.481 eV in case of *meta*-GGA RSCAN and slightly wider bandgap of 1.686 eV was obtained in the case of HSE06. In the next step, we calculated absorption of GdSF crystal. Fig. 5 is Tauc-like plot for indirect transitions where experimental Kubelka-Munk function modified for indirect transition is compared to *meta*-GGA-simulated absorption curve, the latter being modified for indirect transitions, too. Curiously, HSE06 predicting wider formal direct bandgap than *meta*-GGA RSCAN results in almost the same absorption curve like the latter. This comparison evidences no exact quantitative coincidence; however, qualitative agreement is very impressive. Two indirect bandgaps for GdSF can be detected, $E_{g1} = 1.54$ eV and $E_{g2} = 2.4$ eV. The point, where Kubelka-Munk function experiences change from the region of E_{g1} to the region of E_{g2}, is approximately 2.5 eV. The DFT-simulated absorption curve below 2.5 eV exhibits the same slope as the experimental Kubelka-Munk function, and above 2.5 eV its slope experiences twofold increase.

The interpretation of these features are as follows. At 1.54 eV, the direct interband transition to highly dispersive Gd 5d subband is achieved. However, the spectral density of states in this Gd 5d subband is rather small in view of strong dispersion. This is proved by the fact that in Tauc plot for direct transitions there is not any signs of contribution from direct transition at 1.54 eV. As the photon energy increases above 1.54 eV, the transitions become to require the contribution from phonons with the increasing phonon energy, too. When photon energy achieves 2.5 eV, the contribution from less dispersive and more numerous subbands becomes noticeable, thus forming the second bandgap. One more general

statement can be outlined: formally **direct** interband transitions from less dispersive valence subbands to highly dispersive conduction subbands contribute to the **indirect** bandgaps detectable via Tauc plots.

3.3. Microstructures of samples in the GdF₃ – Gd₂S₃ system

The chemical elements Gd, S, F are evenly distributed in the thin section of a single-phase GdSF sample. (Fig. 6 B). Crystals of the GdSF phase are brown in reflected light. The average value of the microhardness of a polycrystalline phase sample is 276 ± 3 HV.

Conclusions about the phase composition of grains in thin sections of samples were made based on the content of chemical elements in grains according to SEM data and the phase composition of samples according to XRD data.

In a sample of eutectic composition, the alternation of the GdF₃ and GdSF grains is clearly observed (Fig. 6 A). In a sample from the region of 50–100 mol. % Gd₂S₃, there are primary grains of the Gd₂S₃ phase located in the field of GdSF phase crystals (Fig. 6C). This distribution of phases unambiguously indicates the formation of the GdSF phase by the reaction of Gd₂S₃ crystals with the melt (Table 4, line 2).

3.4. Thermal characteristics of GdSF, phase transformations in the GdF₃ – Gd₂S₃ system

In the GdF₃ - Gd₂S₃ system, 5 phase transformations were detected by DSC (Fig. 7, Table 4). The temperatures of the α-GdF₃ ⇆ β-GdF₃ polymorphic transition and the melting of GdF₃ within experimental errors (Fig. 7 A) coincide with the data reported in Ref. [12]. On the DSC-curve of α-GdF₃ and samples of the system located near the GdF₃ coordinate, the peak of the thermal effect of the α-GdF₃ ⇄γ-GdF₃ phase transition is present on the heating and cooling curves. When quenching ampoules with GdF₃ samples into saline solutions from temperatures of 1100–1150 °C, the α-GdF₃ modification was obtained. The modification of β-GdF₃ by cooling was not detected. The study of partially oxidized GdF₃₋₂ₓOₓ samples confirmed the data presented in Ref. [15].

The melting peak of the 0.74GdF₃ - 0.26GdSF eutectic has a pronounced linear section that is fully correspondent to the non-variant phase equilibrium in the state diagram of the system (Table 4 line 4, Fig. 7 B, C).

The GdSF compound melts incongruently. The DSC curve recorded the peak of the endothermic thermal effect of the melting of the GdSF phase, as well as the peak of the melting of γ-Gd₂S₃ crystals formed during the decomposition of the GdSF phase (Fig. 7. D).

The melting enthalpy of GdSF was determined by constructing the Tamman triangle for the samples containing 50–97 mol. % Gd₂S₃ (Fig. 7. E, F). In the performance of a DSC analysis, the samples containing 50 mol. % of Gd₂S₃ were melted and then crystallized upon cooling. The samples are primary formed by the γ-Gd₂S₃ crystals surrounded by the GdSF phase. The thin section also contains narrow stripes or triangles of eutectic crystals of the 0.74 GdF₃ + 0.26 GdSF phase (Table 4 line 3), which is in complete agreement with the phase diagram shown in Fig. 8.

The temperatures of congruent melting in the series of compounds LnSF (Ln = La – Sm) regularly decrease [18]. The GdSF compound melts incongruently. An incongruent melting pattern should be predicted for subsequent LnSF compounds of the yttrium subgroup.

The temperature of the α-Gd₂S₃ → γ-Gd₂S₃ polymorphic transition generally coincides with the literature data [17], the enthalpy was determined by the DSC method, and the entropy was calculated. During the transition, a weight loss of up to 0.06% was recorded (Fig. 7. G).

3.5. Phase diagram of the GdF₃ – Gd₂S₃ system

In the GdF₃ - Gd₂S₃ system (Fig. 8), no noticeable areas of solid solutions are formed based on the initial GdF₃ and Gd₂S₃ compounds. In annealed two-phase samples, the unit cell parameters of the GdF₃ and Gd₂S₃ phases, within the limits of the determination errors, coincide with
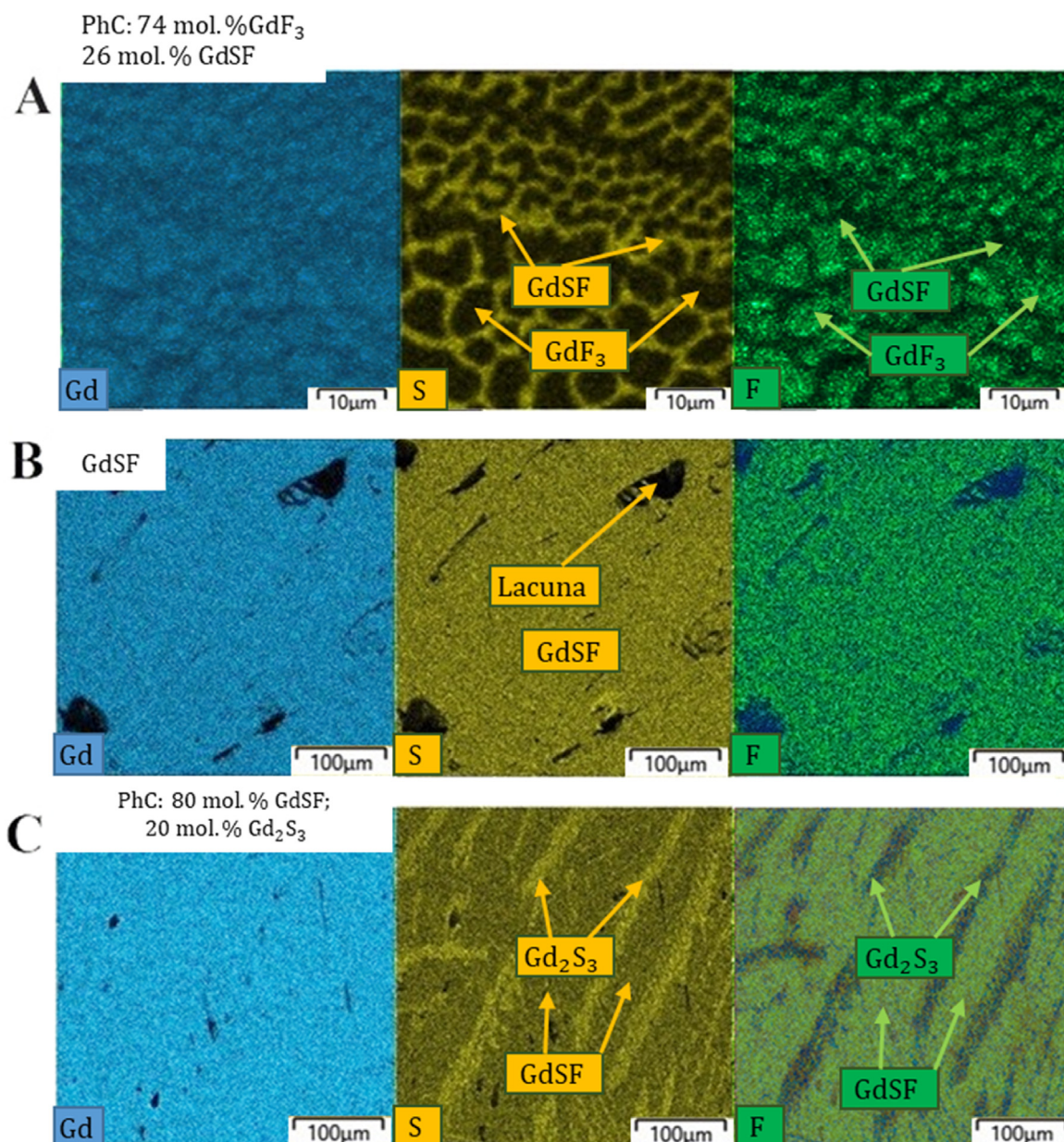
Fig. 6. SEM images of the chemical element contents in thin sections of samples of the GdF_3 - Gd_2S_3 system. The composition of the samples according to the weights of the components: A-13, B-50, C-60 mol. % Gd_2S_3.

Table 4
Temperatures and enthalpies of the phase transformations in the GdF_3-Gd_2S_3 system.

№	Type of phase transformation	Coordinates		Phase transformation equation	ΔH, J/g	ΔH, KJ/mol.	ΔS J/mol
		Comp-ound	t,°C				
1	Polymorph transition	GdF_3	1064 ± 2	α-$GdF_3 \leftrightarrows \beta$-$GdF_3$	11.6 ± 0.8	2.5	1.9
2	Congruent melting	GdF_3	1230 ± 2	β-$GdF_3 \leftrightarrows$ liquid	251.1 ± 17.8	53.8	35.8
3	Incongruent melting	GdSF	1280 ± 2	GdSF $\leftrightarrows$ 0.88 liquid (43 mol. % Gd_2S_3) + 0.12 γ-Gd_2S_3	195 ± 13.6	40.6	26.1
4	Eutectic melting	13 mol. % Gd_2S_3	1182 ± 2	0.74 GdF_3 + 0.26 GdSF $\leftrightarrows$ liquid	169.9 ± 11.9	36.2	24.9
5	Polymorph transition	Gd_2S_3	1217 ± 2	α-$Gd_2S_3 \rightarrow \gamma$-$Gd_2S_3$	37.9 ± 2	15.5	10.4

the crystallochemical parameters of the synthesized GdF_3 and Gd_2S_3 powders.

For samples of the system, changes in the temperatures of polymorphic transitions in GdF_3 and in Gd_2S_3 were not recorded. The DSC curve of the GdF_3 phase sample has a peak at 1064 °C of the α-GdF_3 – β-GdF_3 polymorphic transition. The temperature of the α-$Gd_2S_3 \rightarrow$

γ-Gd_2S_3 transition, according to DSC data, is 1217 °C (Fig. 7 G, Table 4 line 5). In the samples containing more than 95 mol. % of the initial components, the peaks of eutectoid transformations are detected at almost the same temperatures, but at noticeably lower enthalpies.

Between the GdF_3 and GdSF phases, a eutectic is formed with a composition of 0.74 GdF_3 + 0.26 GdSF (in the GdF_3–Gd_2S_3 system, 13
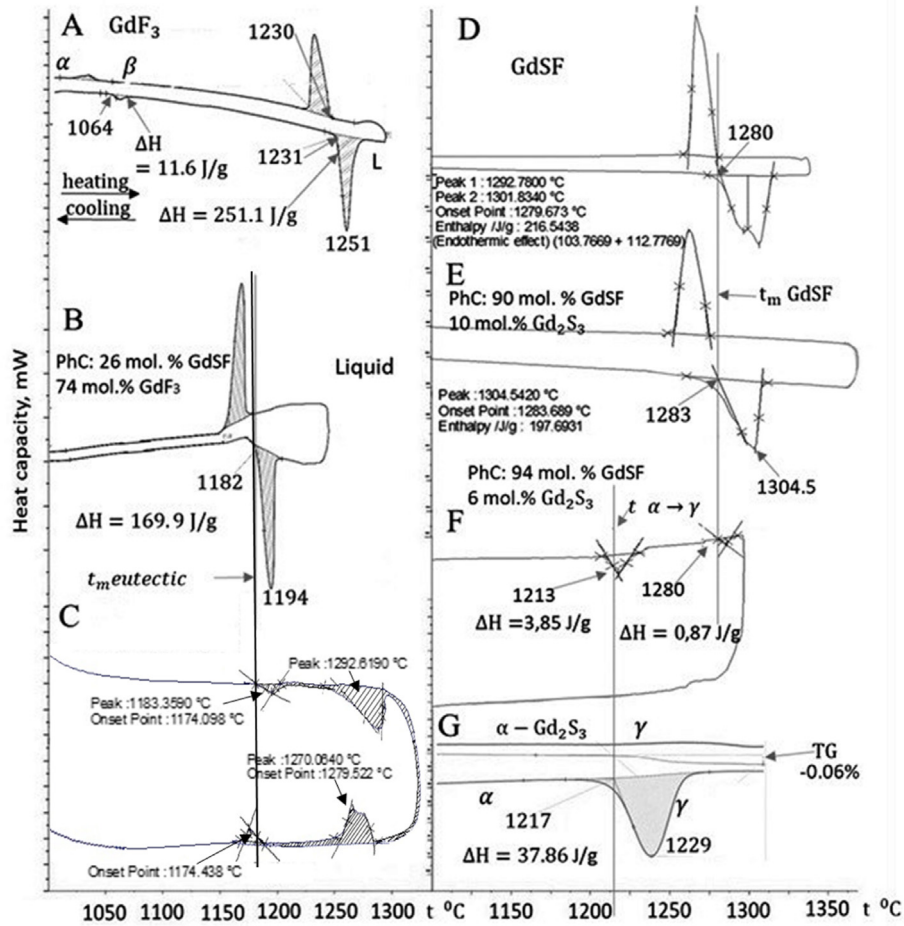
Fig. 7. DSC curves recorded for the samples of the GdF$_3$ - Gd$_2$S$_3$ system. Sample composition: A - GdF$_3$, B - 13, C - 40, D – 50, E − 55; F- 97; G − α − Gd$_2$S$_3$; mol. % Gd$_2$S$_3$. PhC – phase composition of samples.

mol. % Gd$_2$S$_3$). According to DSC data, the melting point of the eutectic is 1182 °C (Fig. 7 B, Table 4 line 4). The obtained data coincide with the results of [8] within the limits of measurement errors. The eutectic is formed by elongated phase crystals, which composition is confirmed by SEM (Fig. 6 A).

In the range of 43–100 mol. % Gd$_2$S$_3$, the DSC curves of the samples show a peak of the thermal endo effect related to the incongruent melting of GdSF (Table 4, Fig. 7). The construction of the Tammann triangle confirms that the peak belongs to the incongruent melting of the GdSF phase Fig. 7 [43].

The GdSF phases are technological materials. In all samples of the system, the GdSF phase is formed in weighted amounts during short annealing (up to 100 h). Samples 50 mol. % Gd$_2$S$_3$ crystallized from the melt and cooled contain more than 99 mol. % GdSF.

Microstructures of the melted two-phase samples crystallized from the melt belonging to the region of 50–100 mol. % Gd$_2$S$_3$ are similar to each other. The samples contain primary Gd$_2$S$_3$ grains of light brown color located in the darker field of the GdSF phase (Fig. 6C). The samples with the phase Gd$_2$O$_2$S were not studied [44].

The liquidus of the system consists of three sections, in each of which from four to seven liquidus temperature values were obtained. (Fig. 8).

3.6. Calculation of the liquidus line of the system according to the Redlich-Kister equation

The Redlich-Kister equation for the molar excess Gibbs energy of a binary solution is converted into an expression for the chemical potentials of the melt components (1, 2). Detailed transformations are pre-

sented in [22].

$$\mu_1 = \mu_1^0 + RT \ln x_1 + (1 - x_1)^2 \left[L_0 + L_1(4x_1 - 1) + L_2(12x_1^2 - 8x_1 + 1) \right], \quad (1)$$

$$\mu_2 = \mu_2^0 + RT \ln x_2 + x_1^2 \left[L_0 + L_1(4x_1 - 3) + L_2(12x_1^2 - 16x_1 + 5) \right] \quad (2)$$

- where x_1 and x_2 are the molar fractions of the components in the melt, γ_1 and γ_2 are the activity coefficients of the 1 st and 2 nd components, L_0, L_1, L_2 are numerical coefficients.

GdF$_3$ was chosen as the first component and Gd$_2$S$_3$ - as the second.

To take into account the features of the phase diagram of the GdF$_3$ - Gd$_2$S$_3$ system, five equations of phase equilibria were compiled in the system: 1) GdF$_3$ phase - eutectic melt, 2) eutectic melt - GdSF phase, 3) melt at the point 43 mol. % Gd$_2$S$_3$ at a temperature of 1280 - GdSF phase, 4) melt at the point 43 mol.% Gd$_2$S$_3$ at a temperature of 1280 °C - Gd$_2$S$_3$ phase, 5) arbitrary equilibrium melt - Gd$_2$S$_3$ phase at 1327°C. For example, in the fifth case, the phase equilibrium equation has the following form (3)

$$\frac{\Delta H_{Gd_2S_3}(T_{Gd_2S_3} - T)}{T_{Gd_2S_3}} =$$
$$- \left[RT \ln x_6 + x_5^2 \left[L_0 + L_1(4x_5 - 3) + L_2(12x_5^2 - 16x_5 + 5) \right] \right] \quad (3)$$

Temperature data on the enthalpies of melting of pure solid components were taken from Refs. [12,17]. When solving a system of five equations, the numerical values of the coefficients were obtained: L$_0$ = −873.064, L$_1$ = 17800, L$_2$ = −14860, and the lines of the liquidus branches were calculated as functions of temperature on composition.
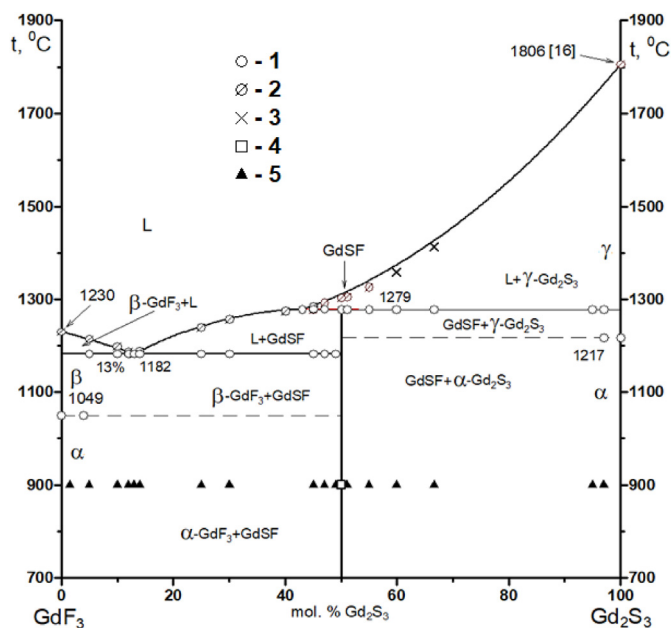
Fig. 8. Phase diagram of the GdF$_3$ – Gd$_2$S$_3$ system. Conventional designations. Differential Scanning Calorimetry data: 1 - peak of thermal effects, phase transformations, which correspond to invariant phase equilibria on the diagram (polymorphic transitions in GdF$_3$, Gd$_2$S$_3$, eutectic melting, incongruent melting of GdSF); 2 - temperature end heat absorption in the sample when it is heated; 3 - complete melt of the sample according to the VPTA data. Phase composition of samples according to XRD, MSA, SEM data: 4 – single-phase; 5 - two-phase. The liquidus line was calculated using the Redlich Kister equation.

The line is shown in Fig. 8. In sections of the GdF$_3$-eutectic liquidus line and the eutectic-peritectic point (43 mol. % Gd$_2$S$_3$), the DSC data and the calculated liquidus line coincide with an accuracy of ±3 °C. In the section of the peritectic-melting point of Gd$_2$S$_3$, the calculated line is mainly located above the experimental points. Probably, when deriving the Redlich-Kister polynomial, an insufficient number of phase equilibria from this region was considered. An approach is being developed to derive the Redlich-Kister polynomial taking into account phase equilibria for all experimentally established liquidus line temperatures.

4. Conclusions

The GdSF phase has the characteristics of ST PbFCl, *P4/nmm, a* (Å) 3.83006(17), *c* (Å) 6.8529(3), *V*(Å^3) 100.527(10), *Z* = 2, microhardness value is 276 ± 3 HV, the optical band gap is Eg = 2.56 eV. The temperature of incongruent melting is equal to GdSF t = 1280 °C, the decomposition enthalpy is ΔH = 40.6 ± 2.8 kJ/mol, ΔS 26.1 ± 1.8 J/mol*K. The phase refers to technological materials. Samples containing 100 mol. % GdSF, obtained by crystallization from the melt, sintering and annealing. Based on the results of studying samples of the GdF$_3$ – Gd$_2$S$_3$ system by DSC, XRD, and SEM methods, a phase diagram of the system was refined. The balance equations for five phase transformations occurring in the system have been compiled. The liquidus line was calculated using the Redlich-Kister equation. The phase diagram of the GdF$_3$ - Gd$_2$S$_3$ system was refined with the consistency of the results of physicochemical methods of analysis based on various physical principles, which allows us to consider the phase diagram of the system reliable.

The temperatures of congruent melting in the series of compounds LnSF (Ln = La – Sm) regularly decrease. The GdSF melts incongruently. The LnSF compounds are stable over time, have a stoichiometric composition. The creation of materials of *p*- and *n*-type conductivity based on GdSF, LnSF is topical.

CRediT authorship contribution statement

M.U. Abulkhaev: Investigation, Validation, Data curation, Visualization, Writing – original draft. **M.S. Molokeev:** Visualization. **A.S. Oreshonkov:** Formal analysis, Methodology. **A.S. Aleksandrovsky:** Formal analysis, Writing – review & editing. **A.V. Kertman:** Writing – original draft, Writing – review & editing, Supervision. **D.N. Kamaev:** Formal analysis, Methodology. **O.V. Trofimova:** Writing – review & editing. **A.V. Elyshev:** Funding acquisition. **O.V. Andreev:** Conceptualization, Supervision, Project administration, Writing – review & editing.

Declaration of competing interest

The authors declare that they have no known competing financial interests or personal relationships that could have appeared to influence the work reported in this paper.

Data availability

No data was used for the research described in the article.

References

[1] D. Pauwels, A. Demourgues, A. Tressaud, Design and optical properties of rare earth-based mixed-anions (O, S, F) compounds, MRS Online Proc. Libr. OPL. 755 (2002) 321–326.

[2] A. Demourgues, A. Tressaud, H. Laronze, P. Macaudière, Rare earth fluorosulfides LnSF and Ln$_2$AF$_4$S$_2$ as new colour pigments, J. Alloys Compd. 323–324 (2001) 223–230, https://doi.org/10.1016/S0925-8388(01)01116-1.

[3] A. Demourgues, A. Tressaud, H. Laronze, P. Gravereau, P. Macaudière, Preparation and structural properties of new series of mixed-anion compounds: rare earth fluorosulfides, J. Fluor. Chem. 107 (2001) 215–221, https://doi.org/10.1016/S0022-1139(00)00361-4.

[4] D. Pauwels, A. Demourgues, H. Laronze, P. Gravereau, F. Guillen, O. Isnard, A. Tressaud, Structural features of new rare earth-based mixed anions (O, S, F) compounds: relationships between optical absorption and rare earth environment, Solid State Sci. 4 (2002) 1471–1479, https://doi.org/10.1016/S1293-2558(02)00038-9.

[5] F. Goubin, X. Rocquefelte, D. Pauwels, A. Tressaud, A. Demourgues, S. Jobic, Y. Montardi, The dielectric function of LnSF rare-earth fluorosulfides (Ln= La, Ce): experiment and theory, J. Solid State Chem. 177 (2004) 2833–2840, https://doi.org/10.1016/j.jssc.2004.05.006.

[6] P. Reynders, S. Bertaux, J.-U. Wichmann, Pearlescent Pigments Based on Fluorides, Oxyfluorides, Fluorosulfides And/or Oxyfluorosulfides, 2004.

[7] J.M. Tomczak, L.V. Pourovskii, L. Vaugier, A. Georges, S. Biermann, Rare-earth vs. heavy metal pigments and their colors from first principles, Proc. Natl. Acad. Sci. USA 110 (2013) 904–907, https://doi.org/10.1073/pnas.1215066110.

[8] E.S. Abdrahmanov, P.O. Andreev, A.N. Boyko, Phase diagrams of systems LnF$_3$–Ln$_2$S$_3$ (Ln = La–Er), Sovremennye neorganicheskie ftoridy, Tr. Tret'ego Mezhdunarod Nogo Sib. Semin. "INTERSIBFLUORINE (2008) 165–167, 2008.

[9] T. Schleid, Drei Formen von Selten-Erd (III)-Fluoridsulfiden: a-LaFS, B-YFS und C-LuFS, Z. Anorg. Allg. Chem. 625 (1999) 1700–1706, https://doi.org/10.1002/(SICI)1521-3749(199910)625:10<1700::AID-ZAAC1700>3.0.CO, 2-5.

[10] I. Ranieri, A. Bressiani, S. Morato, S. Baldochi, The phase diagram of the system LiF–GdF$_3$, J. Alloys Compd. 379 (2004) 95–98, https://doi.org/10.1016/j.jallcom.2004.02.010.

[11] D. de Faoite, I. Tobin, A. Ulyanov, O. Roberts, B. Shortt, L. Hanlon, S. McBreen, K. Stanton, Growth of trigonal gadolinium fluoride in a glass-ceramic for scintillation and optical applications, J. Eur. Ceram. Soc. 38 (2018) 4739–4748, https://doi.org/10.1016/j.jeurceramsoc.2018.05.037.

[12] F. Spedding, D. Henderson, High-temperature heat contents and related thermodynamic functions of seven trifluorides of the rare earths: Y, La, Pr, Nd, Gd, Ho, and Lu, J. Chem. Phys. 54 (1971) 2476–2483, https://doi.org/10.1063/1.1675202.

[13] S. Stankus, R. Khairulin, K. Lyapunov, Phase transitions and thermal properties of gadolinium trifluoride, J. Alloys Compd. 290 (1999) 30–33, https://doi.org/10.1016/S0925-8388(99)00231-5.

[14] I. Ranieri, S. Baldochi, D. Klimm, others, The phase diagram GdF_3-LuF_3, J. Solid State Chem. 181 (2008) 1070–1074, https://doi.org/10.1016/j.jssc.2008.02.017.

[15] B. Sobolev, P. Fedorov, D. Shteynberg, B. Sinitsyn, G. Shakhkalamian, On the problem of polymorphism and fusion of lanthanide trifluorides. I. The influence of oxygen on phase transition temperatures, J. Solid State Chem. 17 (1976) 191–199, https://doi.org/10.1016/0022-4596(76)90220-6.

[16] T. Schleid, Das System Na_zGdClH_x/S II. Einkristalle von Gd_2S_3 im U_2S_3-Typ, Z. F. Anorg. Allg. Chem. 590 (1990) 111–119, https://doi.org/10.1002/zaac.19905900112.

[17] P.O. Andreev, A.A. Polkovnikov, Y.G. Denisenko, O.V. Andreev, T.M. Burkhanova, A.N. Bobylevb, L.A. Pimneva, Temperatures and enthalpies of melting of Ln_2S_3 (Ln= Gd, Tb, Dy, Ho, Er, Tm, Yb, and Lu) compounds, J. Therm. Anal. Calorim. 131 (2018) 1545–1551, https://doi.org/10.1007/s10973-017-6620-x.

[18] P. Andreev, O. Mikhalkina, O. Andreev, A. Elyshev, Enthalpies of melting of LnSF compounds (Ln= La, Ce, Pr, Nd, Sm), Russ. J. Phys. Chem. A 89 (2015) 731–736, https://doi.org/10.1134/S0036024415050040.

[19] P. Andreev, L. Pimneva, Y_2S_3–Y_2O_3 phase diagram and the enthalpies of phase transitions, J. Solid State Chem. 263 (2018) 24–29, https://doi.org/10.1016/j.jssc.2018.03.001.

[20] M.A. Shtykova, V.P. Vorob'eva, P.P. Fedorov, M. Molokeev, A. Aleksandrovsky, A. Elyshev, I. Palamarchuk, I. Yurev, A. Ivanov, N. Habibullayev, others, Features of phase equilibria and properties of phases in the Sb-Sm-Se system, J. Solid State Chem. (2022), 123573, https://doi.org/10.1016/j.jssc.2022.123573.

[21] B.P. Sobolev, High-temperature chemistry of Y, La and lanthanide trifluorides in RF_3–$R'F_3$ systems. Part 2. Phase diagrams of the studied systems, J. Solid State Chem. 298 (2021) 122078, https://doi.org/10.1016/j.jssc.2021.122078.

[22] M. Shtykova, M. Molokeev, B. Zakharov, N. Selezneva, A. Aleksandrovsky, R. Bubnova, D. Kamaev, A. Gubin, N. Habibullayev, A. Matigorov, others, Structure and properties of phases in the Cu2-XSe-Sb2Se3 system. The $Cu_{2-x}Se$-Sb_2Se_3 phase diagram, J. Alloys Compd. 906 (2022), 164384, https://doi.org/10.1016/j.jallcom.2022.164384.

[23] S. Osseni, P. Andreev, A. Polkovnikov, B. Zakharov, A. Aleksandrovsky, M. Abulkhaev, S. Volkova, D. Kamaev, I. Kovenskiy, N. Nesterova, others, Properties of oxysulfide phases and phase diagram of the Nd_2S_3–Nd_2O_3 system, J. Solid State Chem. 314 (2022), 123438, https://doi.org/10.1016/j.jssc.2022.123438.

[24] A. Galler, J. Boust, A. Demourgues, S. Biermann, L.V. Pourovskii, Correlated electronic structure and optical response of rare-earth based semiconductors, Phys. Rev. B 103 (2021) L241105, https://doi.org/10.1103/PhysRevB.103.L241105.

[25] I.A. Razumkova, Y.G. Denisenko, A.N. Boyko, D.A. Ikonnikov, A.S. Aleksandrovsky, N.O. Azarapin, O.V. Andreev, Synthesis and upconversion luminescence in LaF_3: Yb^{3+}, Ho^{3+}, GdF_3: Yb^{3+}, Tm^{3+} and YF_3: Yb^{3+}, Er^{3+} obtained from sulfide precursors, Z. F. Anorg. Allg. Chem. 645 (2019) 1393–1401, https://doi.org/10.1002/zaac.201900204.

[26] O. Andrrev, I. Razumkova, A. Boiko, Synthesis and thermal stability of rare earth compounds REF_3, REF_3-nH_2O and (H_3O) RE_3F_{10}-nH_2O (RE= Tb- Lu, Y), obtained from sulphide precursors, J. Fluor. Chem. 207 (2018) 77–83, https://doi.org/10.1016/j.jfluchem.2017.12.001.

[27] B. Sobolev, Full quasi-system "from LaF_3 to LuF_3" as a combination of 14 binary systems of lanthanide trifluorides with maximal chemical proximity, J. Solid State Chem. 312 (2022), 123163, https://doi.org/10.1016/j.jssc.2022.123163.

[28] T. Schleid, F.A. Weber, C–Gd_2S_3 und C–Tb_2S_3: darstellung und Röntgenstrukturanalyse von Einkristallen, Z. F. Anorg. Allg. Chem. 624 (1998) 557–558, https://doi.org/10.1002/(SICI)1521-3749, 199804)624:4<557::AID-ZAAC557>3.0.CO;2-L.

[29] O.V. Andreev, V.V. Atuchin, A.S. Aleksandrovsky, Y.G. Denisenko, B.A. Zakharov, A.P. Tyutyunnik, N.N. Habibullayev, D.A. Velikanov, D.A. Ulybin, D.D. Shpindyuk, Synthesis, structure, and properties of $EuLnCuSe_3$ (Ln= Nd, Sm, Gd, Er), Crystals 12 (2021) 17, https://doi.org/10.3390/cryst12010017.

[30] S. Landi Jr., I.R. Segundo, E. Freitas, M. Vasilevskiy, J. Carneiro, C.J. Tavares, Use and misuse of the Kubelka-Munk function to obtain the band gap energy from diffuse reflectance measurements, Solid State Commun. 341 (2022), 114573, https://doi.org/10.1016/j.ssc.2021.114573.

[31] S. Rampino, F. Pattini, M. Bronzoni, M. Mazzer, G. Spaggiari, E. Gilioli, $CuSbSe_2$ thin film solar cells with~ 4% conversion efficiency grown by low-temperature pulsed electron deposition, Sol. Energy Mater. Sol. Cells 185 (2018) 86–96, https://doi.org/10.1016/j.solmat.2018.05.024.

[32] S.J. Clark, M.D. Segall, C.J. Pickard, P.J. Hasnip, M.I. Probert, K. Refson, M.C. Payne, First principles methods using CASTEP, Z. F. Krist.-Cryst. Mater. 220 (2005) 567–570, https://doi.org/10.1524/zkri.220.5.567.65075.

[33] M. Cococcioni, S. De Gironcoli, Linear response approach to the calculation of the effective interaction parameters in the LDA+ U method, Phys. Rev. B 71 (2005), 035105, https://doi.org/10.1103/PhysRevB.71.035105.

[34] A.P. Bartók, J.R. Yates, Regularized SCAN functional, J. Chem. Phys. 150 (2019), 161101, https://doi.org/10.1063/1.5128484.

[35] J. Sun, R.C. Remsing, Y. Zhang, Z. Sun, A. Ruzsinszky, H. Peng, Z. Yang, A. Paul, U. Waghmare, X. Wu, others, Accurate first-principles structures and energies of diversely bonded systems from an efficient density functional, Nat. Chem. 8 (2016) 831–836.

[36] D. Pauwels, Cristallochimie des composés de terres rares à anions mixtes. Propriétés d'absorption uv-visible, PhD Thesis, Université Sciences et Technologies-Bordeaux I, 2003.

[37] A.V. Krukau, O.A. Vydrov, A.F. Izmaylov, G.E. Scuseria, Influence of the exchange screening parameter on the performance of screened hybrid functionals, J. Chem. Phys. 125 (2006), 224106, https://doi.org/10.1063/1.2404663.

[38] Y.G. Denisenko, V.V. Atuchin, M.S. Molokeev, A.E. Sedykh, N.A. Khritokhin, A.S. Aleksandrovsky, A.S. Oreshonkov, N.P. Shestakov, S.V. Adichtchev, A.M. Pugachev, Others, Exploration of the crystal structure and thermal and spectroscopic properties of monoclinic praseodymium sulfate $Pr_2(SO_4)_3$, Molecules 27 (2022) 3966, https://doi.org/10.3390/molecules27133966.

[39] E.F. Sinyakova, I.G. Vasilyeva, A.S. Oreshonkov, S.V. Goryainov, N.S. Karmanov, formation of noble metal phases (Pt, Pd, Rh, Ru, Ir, Au, Ag) in the process of fractional crystallization of the $CuFeS_2$ melt, Minerals 12 (2022) 1136, https://doi.org/10.3390/min12091136.

[40] A.S. Oreshonkov, E.V. Sukhanova, Z.I. Popov, Raman spectroscopy of Janus MoSSe monolayer polymorph modifications using density functional theory, Materials 15 (2022) 3988, https://doi.org/10.3390/ma15113988.

[41] V.V. Atuchin, L.I. Isaenko, V.G. Kesler, Z.S. Lin, M.S. Molokeev, A.P. Yelisseyev, S.A. Zhurkov, Exploration on anion ordering, optical properties, and electronic structure in K3WO3F3 elpasolite, J. Solid State Chem. 187 (2012) 159–164, https://doi.org/10.1016/j.jssc.2011.12.037.

[42] Ali H. Reshak, Z.A. Alahmed, J. Bila, Victor V. Atuchin, Bair G. Bazarov, Olga D. Chimitova, Maxim S. Molokeev, Igor P. Prosvirin, Alexander P. Yelisseyev, Exploration of the electronic structure of monoclinic α-$Eu_2(MoO_4)_3$:DFT-based study and X-ray photoelectron spectroscopy, J. Phys. Chem. C 120 (2016) 10559–10568, https://doi.org/10.1021/acs.jpcc.6b01489.

[43] A.V. Ruseikina, O.V. Andreev, E.O. Galenko, S.I. Koltsov, Trends in thermodynamic parameters of phase transitions of lanthanide sulfides $SrLnCuS_3$ (Ln= La–Lu), J. Therm. Anal. Calorim. 128 (2017) 993–999, https://doi.org/10.1007/s10973-016-6010-9.

[44] E. Sal'Nikova, Y. Denisenko, A. Aleksandrovsky, I. Kolesnikov, E. Lähderanta, P. Andreev, N. Azarapin, O. Andreev, S. Basova, A. Matigorov, Synthesis and optical properties RE_2O_2S: Ln (RE= La, Y; Ln= Ce, Eu, Dy, Er), J. Solid State Chem. 279 (2019) 120964, https://doi.org/10.1016/j.jssc.2019.120964.